



Mechanically and electrically nonlinear non-ideal piezoelectric energy harvesting framework with experimental validations

Stephen Leadenham · Alper Erturk 

Received: 20 November 2018 / Accepted: 22 June 2019 / Published online: 5 July 2019
© Springer Nature B.V. 2019

Abstract In the literature of vibration energy harvesting, mechanically nonlinear frameworks have mostly employed linear electrical circuitry to formulate AC input–AC output problems, while the existing efforts on nonlinear power conditioning circuits have assumed linear mechanical behavior. However, even for the simplest case of a stiff (geometrically linear) piezoelectric cantilever, material softening and dissipative nonlinearities in the mechanical domain have to be accommodated to accurately predict the response for moderate to high excitation levels, and likewise a stable DC signal must be obtained to charge a storage component in realistic energy harvesting applications. Furthermore, often times the voltage output is not large enough to assume ideal diode behavior to reduce diodes to switches in AC–DC conversion modeling. Therefore, a relatively complete representation of piezoelectric energy harvesting requires accounting for the mechanical (e.g., material and dissipative) nonlinearities as well as the nonlinear process of AC–DC conversion with non-ideal circuit elements, such as real diodes. To this end, we present and experimentally validate a multiphysics

framework and harmonic balance analysis that combines these mechanical and electrical nonlinear non-ideal effects to predict the DC electrical output (DC voltage across the load) in terms of the AC mechanical input (base vibration) for arbitrary vibration and voltage levels. The focus is placed on a bimorph cantilever with piezoelectric laminates under base excitation. The terminals of the piezoelectric layers are combined in series and connected to a bridge rectifier with non-ideal diodes and a filter capacitor. The multi-term harmonic balance framework can capture the ripple in the DC signal as well as amplitude-dependent nonlinear dynamics accounting for realistic diode behavior. In addition to quantitative comparisons and validations by comparing the experimental data and model simulations, important qualitative trends are unveiled for mechanically and electrically nonlinear non-ideal dynamics of piezoelectric energy harvesting.

Keywords Nonlinear · Vibration · Energy harvesting · Piezoelectricity · Electromechanical systems

S. Leadenham
Lawrence Livermore National Laboratory,
7000 East Avenue, Livermore, California 94550, USA
e-mail: leadenham1@llnl.gov

A. Erturk (✉)
The George W. Woodruff School of Mechanical
Engineering Georgia Institute of Technology,
Atlanta, Georgia 30332, USA
e-mail: alper.erturk@me.gatech.edu

1 Introduction

Research on vibration energy harvesting methods and technologies has received growing attention over the last two decades to enable energy-autonomous low-power systems, such as wireless sensor nodes [1–3]. Among the various approaches for converting ambient vibrations into electricity [4–16], piezoelectric

transduction has been most heavily researched especially due to the high power density and ease of application of piezoelectric materials [17–19].

The most commonly used piezoelectric energy harvester configuration is a cantilever with piezoceramic layers located on a vibrating host structure for electrical power generation from resonant bending vibrations under base excitation. Theoretical and experimental aspects of the linear-resonant cantilever design have been investigated extensively in the existing literature [8–10,20]. Beyond the basic linear dynamics, nonlinear effects in piezoelectric energy harvesting have received dramatically increased attention in the last decade. Three types of basic nonlinearities can be mentioned: (1) designed mechanical nonlinearities (e.g., geometric, magnetoelastic, etc.) for substantial modification (or distortion) of the linear resonance via nonlinear effects and bifurcations [21,22] to enable broadband energy harvesters, leading to a number of efforts to create nonlinear energy harvester configurations (e.g., monostable and bistable Duffing oscillators) via intentionally introduced nonlinearities [23–31]. (2) Additionally, the piezoelectric materials themselves display appreciable inherent nonlinear constitutive and dissipative behavior for moderate to large excitation intensities [32–38]. (3) Thirdly, in order to convert the alternating current produced by a vibrating piezoelectric energy harvester to a form useful for powering electronic devices or charging electrical storage units, rectifiers and regulators must be used to produce a stable voltage and direct current output [39], and other nonlinear circuit opportunities involve nonlinear processing of the piezoelectric output, e.g., via voltage inversion [40].

In the literature of piezoelectric energy harvesting, mechanical and electrical nonlinear effects have so far predominantly been studied separately. Mechanically and electromechanically nonlinear modeling and analysis frameworks [32–38] have employed linear electrical circuitry to formulate AC input–AC output problems, while the existing efforts on modeling and analysis of nonlinear circuits have assumed linear mechanical behavior [41] or idealized rectifier models [40,42,43] that simplify diodes to switches. It is the main goal of this work to explore the combined presence and interactions of inherent mechanical and basic non-ideal circuit nonlinearities through rigorous modeling and experiments within a complete, unified

harmonic balance analysis framework. In the following, a lumped-parameter model of the nonlinear resonant behavior of a vibration energy harvester connected to a bridge rectifier (with non-ideal diodes), filter capacitor, and load resistor is derived. The energy harvester design of interest is a stiff (hence geometrically linear but materially nonlinear) piezoelectric bimorph cantilever with piezoelectric layers connected in series. The problem is explored first to characterize mechanical nonlinearities by exploring the AC input (base excitation) and AC output (voltage across the load) problem in the presence of a resistive load. Linear model parameters are validated for experiments in the linear regime. Material softening and dissipative nonlinearities are identified from nonlinear tests at different excitation levels. Having characterized the mechanical nonlinearities, the AC input–DC output case is studied. For the multiphysics equations of the fully coupled nonlinear system, a harmonic balance solution is applied to analyze the mechanically and electrically nonlinear system dynamics at different excitation levels. Experimental validations are presented, and quantitative and qualitative trends are discussed.

2 Governing nonlinear electromechanical equations

Detailed treatment of the derivation for an electromechanical model of a geometrically linear (stiff) and materially nonlinear bimorph piezoelectric energy harvester and its harmonic balance analysis can be found elsewhere [37] (that work provides a detailed account and justification of the fact that piezoelectric softening is dominantly quadratic, rather than cubic). The piezoceramic cantilever in the experiments of this work is very stiff; hence, the geometric nonlinearities (stiffness hardening and inertial softening) are negligible, whereas material nonlinearity is significant; therefore, the aforementioned modeling approach [37] is suitable (note that geometric nonlinearity can easily be accommodated as needed [38]). After reducing the governing partial differential equations into a lumped-parameter form, the differential equations governing the mechanical and electrical behavior of the energy harvester forced by base excitation (Fig. 1) near a resonance frequency are given by:

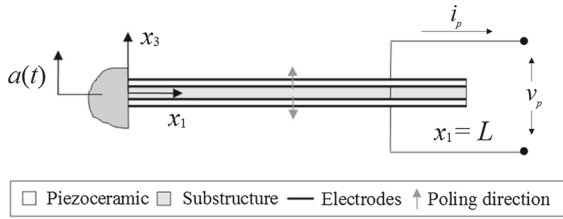


Fig. 1 Schematic of a cantilevered bimorph piezoelectric energy harvester under base excitation (resultant terminals of the electrodes can be connected to a linear/nonlinear circuit)

$$m\ddot{x} + b_1\dot{x} + b_2\dot{x}^2 \operatorname{sgn}(\dot{x}) + k_1x + k_2x^2 \operatorname{sgn}(x) - \theta v_p = -\bar{m}a(t), \tag{1}$$

$$C_p\dot{v}_p + i_p + \theta\dot{x} = 0, \tag{2}$$

where x is the relative transverse displacement of the beam tip with respect to the base, v_p is the electrode voltage, i_p is the electrical current flowing out of the energy harvester, and $a(t)$ is the prescribed base acceleration. The effective beam mass, m , first- and second-order dissipation coefficients, b_1 and b_2 , first- and second-order stiffness coefficients, k_1 and k_2 , electromechanical coupling parameter, θ , forcing mass (due to base excitation), \bar{m} , and capacitance, C_p , are defined in the same way as in [37].

This model includes nonlinearities in the mechanical dissipative and restoring forces (due to b_2 and k_2), but assumes linear electromechanical coupling behavior. As was shown in [37], electromechanical coupling nonlinearities are less important than the dominant mechanical nonlinearities for the electric field levels in energy harvesting. To complete the model, a constitutive relationship between the electrode voltage, v_p , and the harvester output current, i_p , must be defined. The harvester electrodes may be shunted across a load impedance, yielding a linear dynamic constitutive relationship. This allows for the mechanical nonlinearities to be identified and quantified separately from any circuit nonlinearities. For practical use, however, the alternating current produced by the piezoelectric cantilever must be converted to direct current. This process cannot be implemented with linear circuit elements and so will yield a nonlinear constitutive relationship. The following sections deal with modeling the energy harvester connected first to a simple load resistance to identify the mechanical dissipative and elastic nonlinearities, and secondly connected to a practical harvesting circuit using a full-wave diode bridge for rectification.

3 Harvester connected to a load resistance

To study and quantify the mechanical dissipative and elastic nonlinearities contributing to the vibratory behavior of the energy harvester, the electrodes are shunted across a load resistance. This results in the simplest possible constitutive relationship between electrode voltage and current, namely the algebraic equation given by Ohm’s law:

$$v_p = Ri_p. \tag{3}$$

Choosing the electrode voltage to be the electrical state variable and substituting in the above current balance equation yields:

$$C_p\dot{v}_p + \frac{1}{R}v_p + \theta\dot{x} = 0. \tag{4}$$

At low response amplitudes, the dissipative and elastic nonlinearities of this model will disappear, and the steady-state behavior of the system can be found using linear systems theory. Derivations of steady-state solutions in the linear regime will be given first, followed by preparation of the equations for solution by the method of harmonic balance.

3.1 Linear problem

If response amplitudes are restricted to be small, second-order terms in the governing equations can be neglected, yielding the following linear model for a piezoelectric bimorph cantilever excited by transverse base acceleration with electrodes shunted across a load resistance:

$$m\ddot{x} + b_1\dot{x} + k_1x - \theta v_p = -\bar{m}a(t) \tag{5}$$

$$C_p\dot{v}_p + \frac{1}{R}v_p + \theta\dot{x} = 0. \tag{6}$$

To find the complex frequency response functions, which describe the amplitude gain and phase shift of the response signals to harmonic excitation, the following is assumed,

$$a(t) = Ae^{j\Omega t} \tag{7}$$

$$x(t) = Xe^{j\Omega t} \tag{8}$$

$$v_p(t) = V_p e^{j\Omega t}. \tag{9}$$

where j is the unit imaginary number. Substituting the assumed solutions in the linear system and solving for

the complex amplitude ratios yields the solutions for the relative displacement and voltage responses for the vibration harvester connected to a load resistance.

$$\frac{X}{A} = \frac{-\bar{m}(j\Omega RC_p + 1)}{(-\Omega^2 m + j\Omega b_1 + k_1)(j\Omega RC_p + 1) + j\Omega R\theta^2} \quad (10)$$

$$\frac{V_p}{A} = \frac{j\Omega \bar{m} R \theta}{(-\Omega^2 m + j\Omega b_1 + k_1)(j\Omega RC_p + 1) + j\Omega R\theta^2} \quad (11)$$

If dielectric losses are non-negligible and the dielectric loss tangent, $\tan \delta_e$, of the piezoelectric material is available, the capacitance, C_p , may be replaced by a complex capacitance, \tilde{C}_p , defined by:

$$\tilde{C}_p = C_p (1 - j \tan \delta_e). \quad (12)$$

Similarly, if the harvester electrodes are shunted across a more complicated linear circuit, the load resistance, R , need only be replaced by a general complex load impedance, $Z(\Omega)$. Additionally, the kinematic response signal measured in experiments is the cantilever tip velocity in the inertial frame rather than relative tip displacement. Modifying the frequency response functions to include dielectric losses and correspond to experimentally measured signals yields the following expressions, with \dot{X}_I representing the complex velocity amplitude measured in the inertial frame.

$$\frac{\dot{X}_I}{A} = \frac{-j\Omega \bar{m}(j\Omega R \tilde{C}_p + 1)}{(-\Omega^2 m + j\Omega b_1 + k_1)(j\Omega R \tilde{C}_p + 1) + j\Omega R\theta^2} + \frac{1}{j\Omega} \quad (13)$$

$$\frac{V_p}{A} = \frac{j\Omega \bar{m} R \theta}{(-\Omega^2 m + j\Omega b_1 + k_1)(j\Omega R \tilde{C}_p + 1) + j\Omega R\theta^2} \quad (14)$$

By comparing these to experimentally generated frequency response functions, the quality of first principles predictions (for low amplitudes) can be evaluated, and model parameters can be updated.

3.2 Mechanically nonlinear, electrically linear problem

To study the steady-state behavior of the governing equations for moderate to large response amplitudes

in a stiff cantilever (for which geometric nonlinearities are negligible), material nonlinearities in the form of the second-order dissipation and stiffness terms are retained, and the excitation due to the base acceleration is restricted to be periodic. As is commonly done, the case of pure harmonic excitation is examined for simplicity. Because the system is nonlinear, superposition no longer holds, and therefore, the governing equations must be real valued. To include dielectric loss, the imaginary portion of the current flowing through the capacitor due to the loss tangent is recognized to act like an additional parasitic resistance in parallel with the load resistance. The governing equations for the nonlinear behavior of a piezoelectric bimorph excited by a harmonic base acceleration with electrodes connected to a load resistance can therefore be expressed as:

$$m\ddot{x} + b_1\dot{x} + b_2\dot{x}^2 \operatorname{sgn}(\dot{x}) + k_1x + k_2x^2 \operatorname{sgn}(x) - \theta v_p = -\bar{m}A \cos(\Omega t) \quad (15)$$

$$C_p \dot{v}_p + \left(\Omega C_p \tan \delta_e + \frac{1}{R} \right) v_p + \theta \dot{x} = 0 \quad (16)$$

Nonlinear differential equations can be simulated using numerical integrators, but the presence of transient responses can make numerical integrators slow to find steady-state behavior, especially when the system is lightly damped. Numerical methods that find periodic steady-state solutions directly, while accounting for higher harmonics, are therefore preferable (e.g., the harmonic balance method). To prepare the governing equations for numerical simulation of any kind, it is useful to put the system in state space form and is advantageous to nondimensionalize it. To this end, the nondimensional state space system is defined as:

$$\mathbf{u}' = \mathbf{f}(\tau, \mathbf{u}), \quad (17)$$

where \mathbf{u} is the nondimensional state vector and $()'$ denotes the derivative with respect to nondimensional time, τ . The system is nondimensionalized by defining characteristic time, length, and voltage scales (T_c , L_c , and V_c) accordingly.

$$t = T_c \tau, \quad v_p = V_c u_3, \quad \dot{v}_p = \frac{V_c}{T_c} u'_3, \quad (18)$$

$$x = L_c u_1, \quad \dot{x} = \frac{L_c}{T_c} u_2, \quad \ddot{x} = \frac{L_c}{T_c^2} u'_2.$$

Substituting these in the governing equations yields:

$$m \frac{L_c}{T_c^2} u_2' + b_1 \frac{L_c}{T_c} u_2 + b_2 \left(\frac{L_c}{T_c} u_2 \right)^2 \text{sgn}(u_2) + k_1 L_c u_1 + k_2 (L_c u_1)^2 \text{sgn}(u_1) - \theta V_c u_3 = -\bar{m} A \cos(\Omega T_c \tau) \tag{19}$$

$$C_p \frac{V_c}{T_c} u_3' + \left(\Omega C_p \tan \delta_e + \frac{1}{R} \right) V_c u_3 + \theta \frac{L_c}{T_c} u_2 = 0, \tag{20}$$

which can be rearranged into state space form to give:

$$\begin{aligned} f_1 &= u_1' = u_2 \\ f_2 &= u_2' = - \left(\frac{k_1 T_c^2}{m} \right) u_1 - \left(\frac{k_2 L_c T_c^2}{m} \right) u_1^2 \text{sgn}(u_1) - \left(\frac{b_1 T_c}{m} \right) u_2 - \left(\frac{b_2 L_c}{m} \right) u_2^2 \text{sgn}(u_2) + \left(\frac{\theta V_c T_c^2}{m L_c} \right) u_3 - \left(\frac{\bar{m} A T_c^2}{m L_c} \right) \cos(\Omega T_c \tau) \\ f_3 &= u_3' = - \left(\frac{\theta L_c}{C_p V_c} \right) u_2 - \left(\Omega T_c \tan \delta_e + \frac{T_c}{R C_p} \right) u_3 \end{aligned} \tag{21}$$

For the method of harmonic balance, the Jacobian matrix of the system is required, whose elements are defined by the expression:

$$J_{ij} = \frac{\partial f_i}{\partial u_j} \tag{22}$$

Details and examples of implementing a multi-term harmonic balance solution (obtaining the nonlinear algebraic equations by Galerkin’s weighted residual minimization and then applying a multivariate Newton-Raphson scheme) in energy harvesting problems can be found elsewhere [31,37].

4 Harvester connected to a rectification circuit with non-ideal diodes

For practical energy harvesting purposes, a stable DC output is required to charge a storage component or to power an electronic device. Since a vibration energy harvester naturally produces AC, the output current must be rectified and conditioned. The simplest passive way of accomplishing this is with a diode bridge

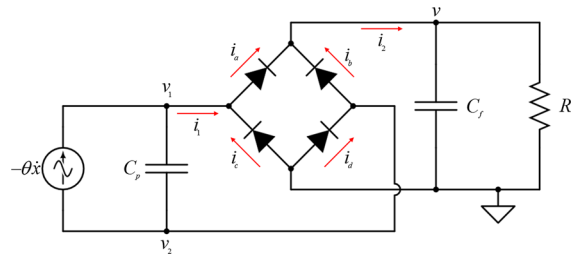


Fig. 2 Circuit diagram of piezoelectric energy harvester connected to a bridge rectifier, filter capacitor, and load resistance. Currents and node voltages used for model derivations are labeled

and filter capacitor. A diagram of a piezoelectric energy harvester connected to such a circuit is shown in Fig. 2.

On the left side of the bridge is the piezoelectric energy harvester modeled by a dependent current source coupled to the structure motion and the capacitance of the piezoelectric material. On the right-hand side of the diode bridge are the filter capacitor and a load resistance. Since for practical purposes the DC power is the quantity of interest, and the filter capacitor is properly large, any reactance of the load can be neglected. Node voltages and currents needed to derive the governing equations are labeled. By applying Kirchhoff’s current law, the following expressions relating currents can be found.

$$i_1 = -\theta \dot{x} - C_p (\dot{v}_1 - \dot{v}_2) = i_a - i_c = i_d - i_b \tag{23}$$

$$i_2 = C_f \dot{v} + \frac{1}{R} v = i_a + i_b = i_c + i_d \tag{24}$$

In order to find the governing equations in terms of node voltages, a relationship between the voltage across a diode and the current flowing through it is required. For its combination of simplicity and smoothness, the Shockley diode model is used:

$$i_D = I_s \left[\exp \left(\frac{v_D}{n V_T} \right) - 1 \right] \tag{25}$$

The Shockley diode model relates the voltage across the diode, v_D , to the current flow, i_D . It is parameterized by the saturation current, I_s , and the product of the ideality factor and the thermal voltage, $n V_T$. The saturation current is the current that will flow backward through the diode when a large reverse voltage is applied and is on the order of 10^{-12} A. A real diode has a reverse breakdown voltage at which large amounts of reverse current will flow. By using the Shockley model,

it is assumed that the diode bridge is properly chosen to avoid breakdown. The thermal voltage is defined as $V_T = k_B T/q$ (where k_B is Boltzmann’s constant, T is the operating temperature, and q is the electron charge) and is approximately 26 mV at room temperature. Using the Shockley model, the four diode currents can be expressed as:

$$\begin{aligned} i_a &= I_s \left[\exp\left(\frac{v_1 - v}{nV_T}\right) - 1 \right] \\ i_b &= I_s \left[\exp\left(\frac{v_2 - v}{nV_T}\right) - 1 \right] \\ i_c &= I_s \left[\exp\left(\frac{-v_1}{nV_T}\right) - 1 \right] \\ i_d &= I_s \left[\exp\left(\frac{-v_2}{nV_T}\right) - 1 \right] \end{aligned} \tag{26}$$

Since the Shockley model is an algebraic model for the current–voltage characteristic of a diode, it can be shown that the mean potential on the input terminals of the diode bridge must always equal the mean potential on the output terminals. This yields the relations:

$$\begin{aligned} v_p &= v_1 - v_2, \quad v = v_1 + v_2, \\ v_1 &= \frac{v + v_p}{2}, \quad v_2 = \frac{v - v_p}{2}, \end{aligned} \tag{27}$$

which reduces the number of voltage that define the system from three to two, being the voltage across the electrodes of the piezoelectric cantilever, v_p as before, and the voltage across the load resistance, the negative terminal of which is grounded. Substituting the expressions for the diode currents and node voltages, v_1 and v_2 , allows simplification of the current balance equations. The current balance equation involving the current flowing into the diode bridge is given by:

$$C_p \dot{v}_p + \theta \dot{x} + 2I_s \sinh\left(\frac{v_p}{2nV_T}\right) \exp\left(\frac{-v}{2nV_T}\right) = 0 \tag{28}$$

Likewise the current balance equation involving current flowing out of the bridge is given by:

$$C_f \dot{v} + \frac{1}{R} v + 2I_s \left[1 - \cosh\left(\frac{v_p}{2nV_T}\right) \exp\left(\frac{-v}{2nV_T}\right) \right] = 0 \tag{29}$$

Combining these current balance equations with the differential equation governing the mechanical behavior

above yields a model describing the dynamics of a piezoelectric cantilever undergoing harmonic base acceleration excitation with electrodes connected to the input terminals of a diode bridge, the output terminals of which are connected to a filter capacitor and load resistor in parallel. As before, dielectric losses in the piezoelectric material are included.

$$m\ddot{x} + b_1 \dot{x} + b_2 \dot{x}^2 \operatorname{sgn}(\dot{x}) + k_1 x + k_2 x^2 \operatorname{sgn}(x) - \theta v_p = -\bar{m}A \cos(\Omega t) \tag{30}$$

$$C_p \dot{v}_p + \Omega C_p \tan \delta_e v_p + \theta \dot{x} + 2I_s \sinh\left(\frac{v_p}{2nV_T}\right) \exp\left(\frac{-v}{2nV_T}\right) = 0 \tag{31}$$

$$C_f \dot{v} + \frac{1}{R} v + 2I_s \left[1 - \cosh\left(\frac{v_p}{2nV_T}\right) \times \exp\left(\frac{-v}{2nV_T}\right) \right] = 0 \tag{32}$$

From these equations, one can make qualitative descriptions of the system behavior. First, the equations are heavily biased in favor of positive values of the output voltage, v , due to the presence of the exponential functions. Secondly, the equation governing the evolution of the piezoelectric electrode voltage, v_p , is an odd function of v_p due to the hyperbolic sine function, while the equation governing the evolution of the output voltage, v , is an even function of v_p due to the hyperbolic cosine function. Both of these observations are consistent with an intuitive understanding of current rectification. As before, it is advantageous to nondimensionalize and cast the system in state space form. The same nondimensionalization and state representation as in Sect. 3.2 are used, with the addition of a fourth state representing the output voltage.

$$v = V_c u_4, \quad \dot{v} = \frac{V_c}{T_c} u'_4 \tag{33}$$

Substituting the nondimensional state definitions in the system yields the same result for the mechanical governing equation, but new expressions for the electrical governing equations:

$$\begin{aligned} C_p \frac{V_c}{T_c} u'_3 + \Omega C_p \tan \delta_e V_c u_3 + \theta \frac{L_c}{T_c} u_2 \\ + 2I_s \sinh\left(\frac{V_c u_3}{2nV_T}\right) \exp\left(\frac{-V_c u_4}{2nV_T}\right) = 0 \end{aligned} \tag{34}$$

$$C_f \frac{V_c}{T_c} u_4' + \frac{1}{R} V_c u_4 + 2I_s \left[1 - \cosh \left(\frac{V_c u_3}{2nV_T} \right) \times \exp \left(\frac{-V_c u_4}{2nV_T} \right) \right] = 0, \tag{35}$$

which can be arranged into state space form:

$$\begin{aligned} f_1 &= u_1' = u_2 \\ f_2 &= u_2' = \\ &\quad - \left(\frac{k_1 T_c^2}{m} \right) u_1 - \left(\frac{k_2 L_c T_c^2}{m} \right) u_1^2 \operatorname{sgn}(u_1) \\ &\quad - \left(\frac{b_1 T_c}{m} \right) u_2 - \left(\frac{b_2 L_c}{m} \right) u_2^2 \operatorname{sgn}(u_2) \\ &\quad + \left(\frac{\theta V_c T_c^2}{m L_c} \right) u_3 - \left(\frac{\bar{m} A T_c^2}{m L_c} \right) \cos(\Omega T_c \tau) \\ f_3 &= u_3' = - \left(\frac{\theta L_c}{C_p V_c} \right) u_2 - (\Omega T_c \tan \delta_e) u_3 \\ &\quad - \left(\frac{2I_s T_c}{C_p V_c} \right) \sinh \left[\left(\frac{V_c}{2nV_T} \right) u_3 \right] \\ &\quad \times \exp \left[- \left(\frac{V_c}{2nV_T} \right) u_4 \right] \\ f_4 &= u_4' = - \left(\frac{2I_s T_c}{C_f V_c} \right) \left\{ 1 - \cosh \left[\left(\frac{V_c}{2nV_T} \right) u_3 \right] \right. \\ &\quad \left. \times \exp \left[- \left(\frac{V_c}{2nV_T} \right) u_4 \right] \right\} - \left(\frac{T_c}{RC_f} \right) u_4 \end{aligned} \tag{36}$$

The Jacobian matrix is defined as previously.

5 Experimental investigation

To verify the validity of the proposed model for the full nonlinear dynamics of a practically realized piezoelectric vibration harvester, a set of three types of experiments are conducted. First, the energy harvester is connected directly to a set of load resistances, ranging from near short circuit to near open circuit, and excited at low enough base acceleration levels to remain in the linear behavior regime (linear experiments). By comparing the predictions of the linear model to experimental frequency response functions, linear model parameters can be validated/identified. Secondly, the energy harvester is excited by frequency sweeps at various constant base acceleration amplitudes while still connected to the same set of load resistors (AC–AC experiments). By comparing the predictions of the nonlinear mechanical model to experimental frequency response curves,

the parameters governing the nonlinear mechanical dissipation and nonlinear stiffness can be identified. Third, the energy harvester is connected to a bridge rectifier, filter capacitor, and load resistance to approximate practical energy harvesting operation (AC–DC experiments). Excitation for the AC–DC experiments is the same as for the AC–AC experiments. Load resistance values are the same for all three experiment types.

5.1 Experimental setup

The piezoelectric energy harvester tested consists of a PZT-5A piezoelectric bimorph cantilever manufactured Piezo Systems, Inc. mounted in a custom fixture with conductive jaws electrically insulated from the rest of the clamp forming the two electrodes. The two piezoelectric layers are poled in opposite directions and are electrically connected in series. A microscope photograph displaying the central brass substrate and upper and lower piezoelectric laminates is shown as an inset in Fig. 3.

For base excitation experiments, the fixture is attached to the armature of a Brüel and Kjær Type

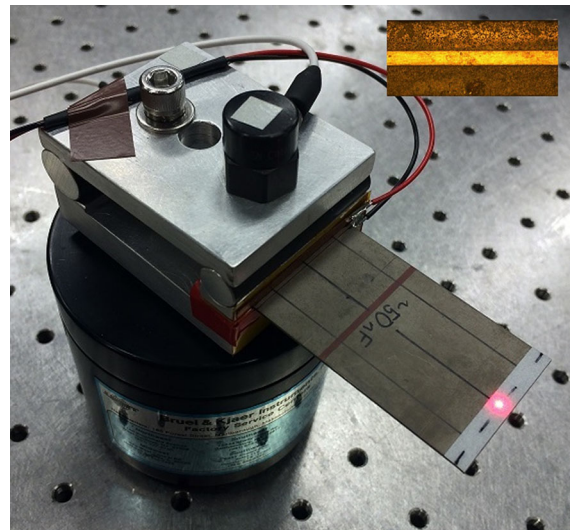


Fig. 3 Close-up photograph of the experimental setup along with an inset showing a microscopic photograph of the edge view: The brass substrate is the light colored central layer, sandwiched by two PZT-5A piezoceramic layers. The piezoelectric bimorph cantilever is fixed in a custom clamp mounted to the shaker with an attached accelerometer. The upper and lower clamp jaws contact the nickel electrode plating on the top and bottom surfaces of the cantilever forming the electrodes. Retroreflective tape is placed near the tip of the cantilever to facilitate laser Doppler vibrometer measurements

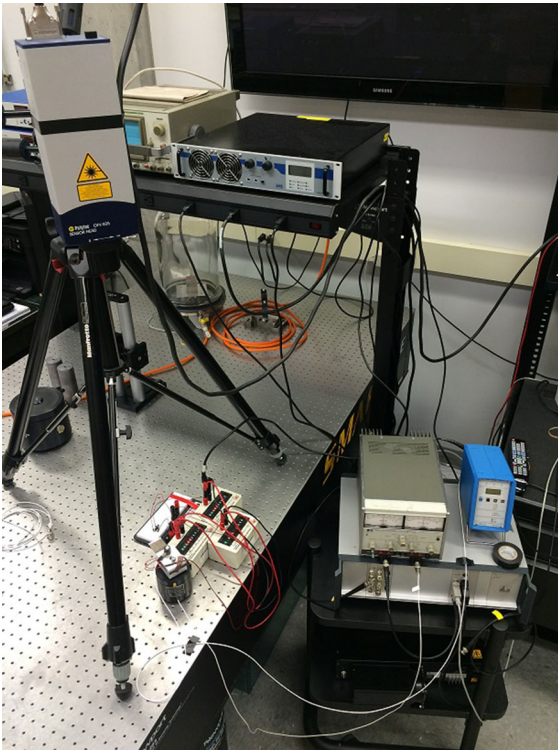


Fig. 4 Overview photograph of the experimental setup. The laser Doppler vibrometer, vibration controller, power amplifier, accelerometer signal conditioner, resistance and capacitance substitution boxes, and breadboard for the rectification circuit are shown

4810 mini shaker powered by an Hewlett Packard 6826A power supply and amplifier. Frequency sweeps at constant base acceleration amplitude are conducted using a SPEKTRA VCS201 vibration control system using acceleration feedback. The base acceleration signal is measured using a Kistler 8636C5 piezoelectric accelerometer powered and conditioned by a Type 5134 power supply and coupler. Load resistance and filter capacitor values are varied using IET Labs RS-201W and CS-301L resistance and capacitance substitution boxes, respectively. Rectification is done using a Diodes Incorporated model KBP202G bridge rectifier. Tip velocity measurements are taken using a Polytec OFV-505 laser Doppler vibrometer and OFV-5000 controller. Data are collected using National Instruments models 9215 and 9223 data acquisition units and SignalExpress software. For linear regime tests, the excitation signal sent to the amplifier is generated by an NI 9263 analog output module. Photographs of the experimental setup are shown in Figs. 3 and 4.

5.2 Linear regime experiments with AC–AC circuit

Linear regime experiments generate measured frequency response functions relating the input base acceleration to the outputs of cantilever tip velocity measured in the inertial frame and the voltage across the load resistance. The set of load resistances consists of 13 resistance values ranging logarithmically from $1\text{ k}\Omega$ to $1\text{ M}\Omega$ (covering a broad range between short- and open-circuit conditions). From the measured voltage frequency response function, current and power frequency response functions can be calculated. The excitation for the linear regime experiments consists of a rectangular white noise signal. Multiple averages are taken. The base acceleration level is kept low to ensure system behavior is linear, with an RMS (root mean square) value of the base acceleration noise signal of approximately 0.01 g .

Figure 5 shows a comparison between the measured experimental tip velocity and electrode voltage, calculated experimental current and power frequency response functions, and predictions from the linear models given above. Experimental data are shown by markers and model predictions by curves (in these and following figures). Each color corresponds to a different resistance value, with black markers in the experimental velocity frequency response plot indicating true short circuit, with a peak near 115 Hz , and true open-circuit conditions, with a peak near 120 Hz . First principles geometric and model parameters are based on distributed-parameter modeling or identified from experiments as required. Geometric and material properties of the bimorph needed for the linear model can be found in Table 1.

Model predictions match very well with experimental data. It is notable that this energy harvester shows two separate maxima in the power generation frequency response function: one at a small load resistance value (near-short-circuit conditions with a lower frequency of the peak) and one at a large load resistance value (near open circuit with a higher frequency of the peak). This is characteristic of electromechanical resonant systems that have a large relative degree of electromechanical coupling and sufficiently low damping [2, 42]. In the linear regime, the two power generation maxima are distinct, but will tend to coalesce for larger excitation levels as will be discussed further in Sect. 6.1. For an ideal piezoelectric material with no dielectric loss, the two peaks in power generation would be of

Fig. 5 AC input–AC output test data and model in the linear response regime with various load resistance values. Experimental data shown with markers and model predictions shown with curves. Black markers in the vibration frequency response show the true short- and open-circuit cases

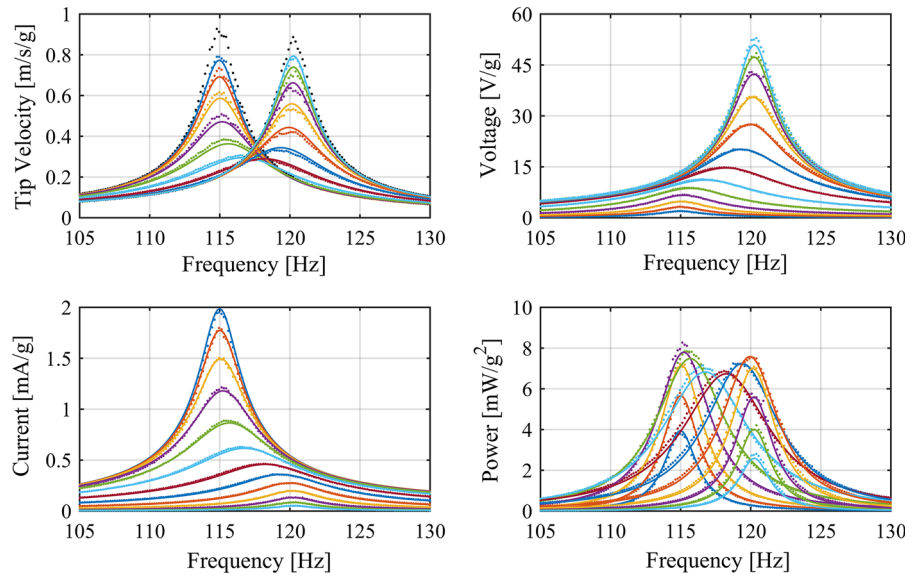


Table 1 Material and geometric parameters for the brass-reinforced PZT-5A bimorph cantilever (Piezo Systems, Inc. model number T226-A4-503X)

PZT density	ρ_p	7800	kg
PZT elastic modulus	c_{11}	66	GPa
PZT loss factor	γ_1	0.021	
Coupling	e_{31}	-14.4	C/m ²
Permittivity	ϵ_{33}	14.2	nF/m
Brass density	ρ_s	8500	kg
Brass elastic modulus	c_s	100	GPa
Overhang length	l	51.9	mm
Total length	l_e	63.7	mm
Width	b	31.8	mm
PZT thickness (each)	h_p	0.267	mm
Brass thickness	h_s	0.127	mm

the same magnitude. For this energy harvester, dielectric loss is significant, and so the peak power point near open circuit conditions, which experiences higher voltages, is lower in magnitude than the near-short-circuit peak power point.

5.3 Nonlinear regime experiments

Nonlinear regime experiments consist of frequency sweep tests at constant acceleration levels of 0.1, 0.2, and 0.3 g RMS. Tests at each acceleration level were

repeated for the same 13 load resistance values, ranging from 1 k Ω to 1 M Ω , used in the linear regime experiments. The maximum base acceleration amplitude of 0.3 g RMS is chosen to keep the cantilever tip deflection within the safe limits provided by the manufacturer. This choice of base acceleration level corresponds to a safety factor of approximately two for the maximum tip displacement. The frequency sweep rate for each test must be slow enough for the test to occur at quasi-steady state. Each data point in the experimental frequency response curves is the result of an average of approximately 100 cycles. Mechanically nonlinear regime experiments are first conducted for the AC–AC circuit configuration, which is the same as in the linear regime experiments, and then followed by the AC–DC circuit configuration with rectification. To allow direct comparisons of behavior with and without the electrical nonlinearities caused by rectification, the nonlinear mechanical and fully nonlinear test cases are conducted with the same set of base acceleration amplitudes.

5.3.1 AC–AC circuit configuration: mechanically nonlinear and electrically linear problem

Plots of experimental data and model predictions are shown in Figs. 6, 7 and 8. RMS tip velocity, RMS voltage, RMS current, and average power are shown. Colors again correspond to the load resistance value and match those of the linear regime tests. Model predictions are generated using the model given above solved

Fig. 6 AC–AC test data and model at 0.1 g RMS with various load resistance values. Experimental data shown with markers and model predictions shown with curves

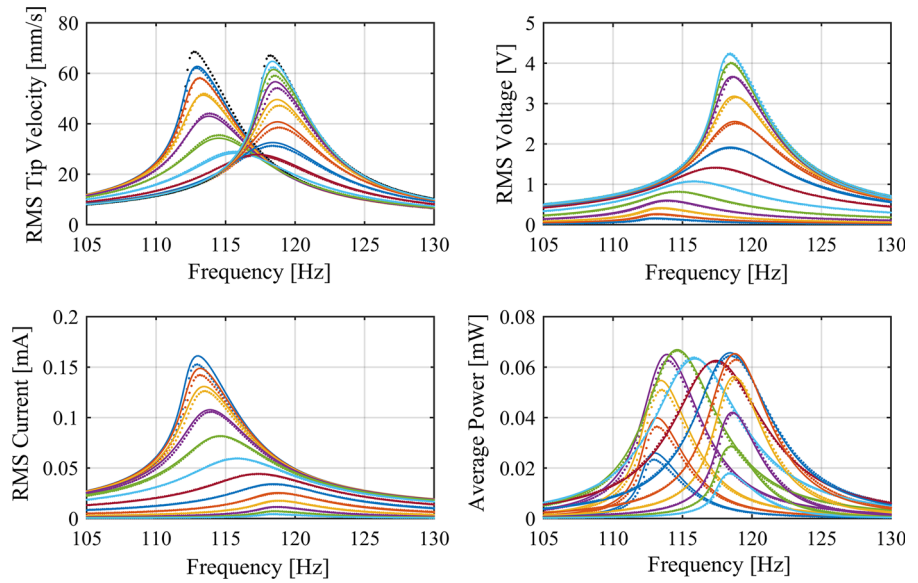
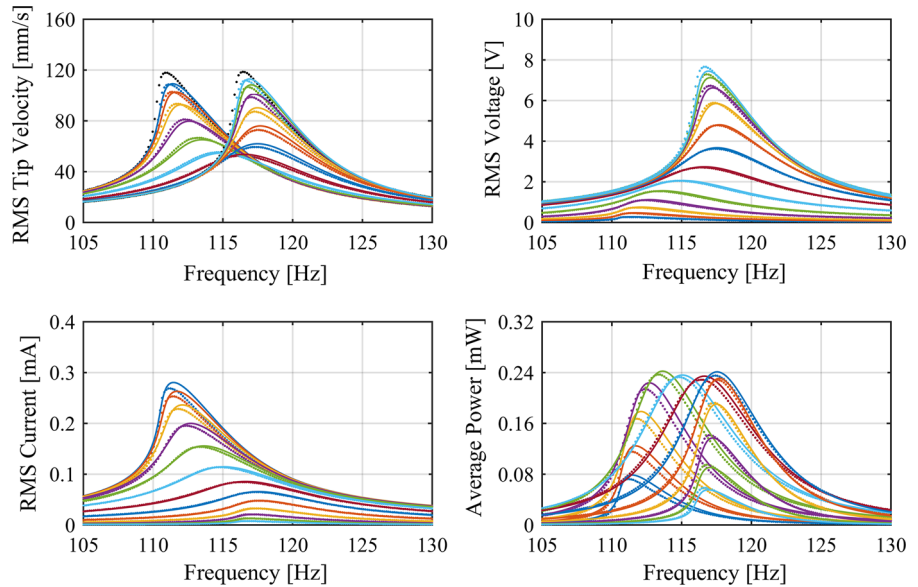


Fig. 7 AC–AC test data and model at 0.2 g RMS with various load resistance values. Experimental data shown with markers and model predictions shown with curves



using a general numerical harmonic balance solver. By comparing the predictions of the nonlinear mechanical model to experimental frequency response curves, the parameters governing the nonlinear mechanical dissipation and nonlinear stiffness can be identified. The parameters defining the nonlinear mechanical behavior are shown in Table 2.

Again there is good agreement between model predictions and experimental results. As the model is a relatively simple model including only nonlinearities in the mechanical dissipation and stiffness, it is most

accurate for lower excitation amplitudes and loses some accuracy as the excitation amplitude increases. In these plots, the limits of the vertical axis scale with the excitation amplitude. The effect of the nonlinear mechanical dissipation can be seen in the decrease in the response amplitude relative to the excitation amplitude with growing base acceleration level. The effect of the nonlinear stiffness can be seen in the shifts of the short-circuit and open-circuit resonant peaks. Short-circuit and open-circuit resonant peaks shift from approxi-

Fig. 8 AC–AC test data and model at 0.3 g RMS with various load resistance values. Experimental data shown with markers and model predictions shown with curves

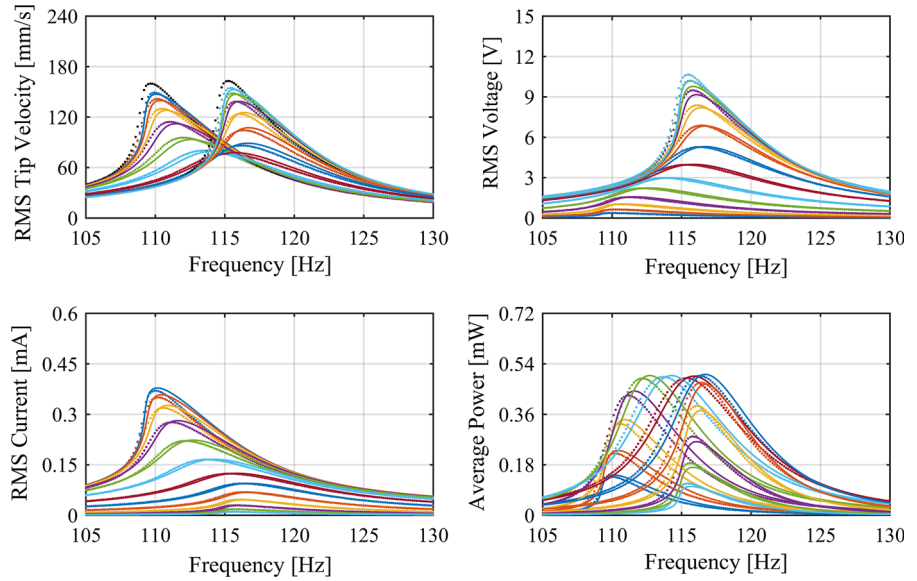


Table 2 Identified quadratic elastic modulus and loss factor

Second-order modulus	c_{nl}	− 83	TPa
Second-order loss factor	γ_{nl}	0.15	

mately 115 and 120 Hz in the linear regime to 110 and 115 Hz at 0.3 g RMS, respectively.

5.3.2 AC–DC circuit configuration: mechanically and electrically nonlinear non-ideal problem

For the AC–DC experiments, the steady-state output voltage depends on both the filter capacitance and the load resistance. As in the linear and AC–AC experiments, the mean power generation level and resonant frequency depend on the load resistance. Additionally, the amount of unwanted ripple in the load voltage and current depends on the time constant of the output, namely the product RC_f . The ripple factor is defined as:

$$RF = \frac{\sqrt{V_{RMS}^2 - V_{DC}^2}}{|V_{DC}|}$$

The larger the value of the time constant, RC_f , the smaller the amount of ripple. This is desirable, and so a practical energy harvester would have a value for RC_f significantly larger than the ripple period. Experimentally, frequency sweep tests are conducted at quasi-steady state, and so the frequency sweep rate of the

must change inversely proportional to the output time constant. Therefore, to ensure that the single sweep rate also used in the AC–AC experiments will be slow enough for all tests without making them unnecessarily lengthy, filter capacitor values are chosen for each of the load resistance values to make the output time constant always 0.01 seconds, or approximately two times the period of the ripple current. This means that for load resistance values ranging from 1 kΩ to 1 MΩ, filter capacitor values vary from 10μF to 10nF.

Plots of experimental data and model predictions are shown in Figs. 9, 10 and 11. RMS tip velocity, DC output voltage, DC current, and average power are shown. Colors again correspond to the load resistance value and match those of the linear regime tests and AC–AC experiments. Model predictions are generated using the fully nonlinear model given above solved using a general numerical harmonic balance solver. By comparing the predictions of the fully nonlinear model to experimental frequency response curves, the parameters governing the rectification circuit can be identified. The parameters defining the rectification nonlinearity are shown in Table 3. The values used are typical values for silicon diodes and did not require any updating.

The fully nonlinear model agrees well with experimental results to predict trends and behavior of a practically realized piezoelectric vibration energy harvester. The most important qualitative differences between the AC–AC and AC–DC behavior of the energy harvester can be seen in the tip velocity and power generation fre-

Fig. 9 AC–DC test data and model at 0.1 g RMS with various load resistance values. Experimental data shown with markers and model predictions shown with curves

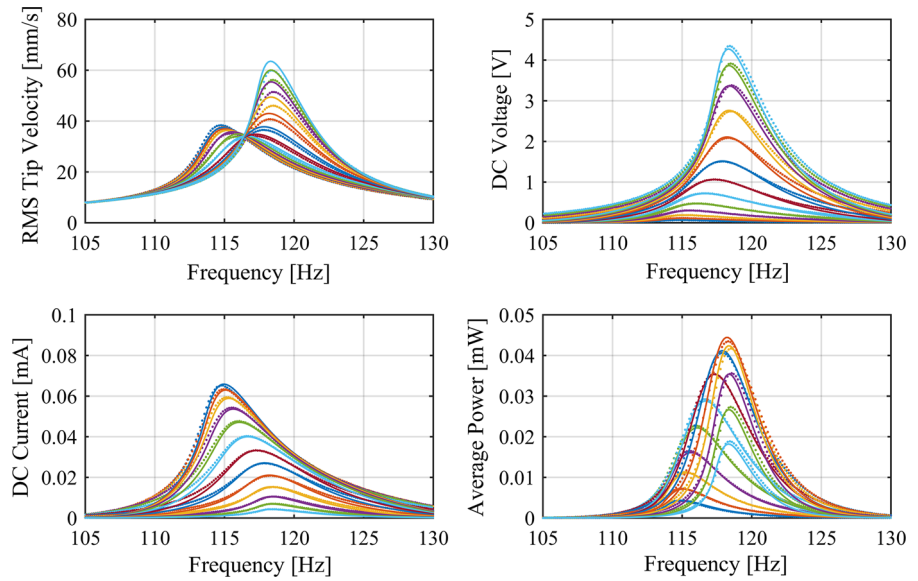
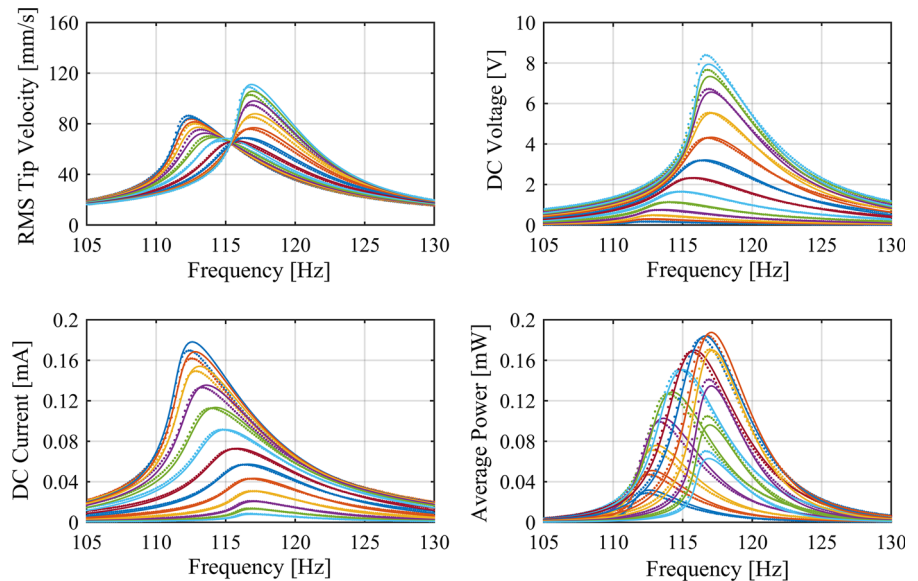


Fig. 10 AC–DC output test data and model at 0.2 g RMS with various load resistance values. Experimental data shown with markers and model predictions shown with curves



quency response curves. In the velocity response, the magnitude of the near-short-circuit resonance is greatly reduced compared to the near-open-circuit response. In the AC–AC experiments, the amplitudes of the velocity response are very similar between near-short-circuit and near-open-circuit conditions. In the power generation response, the curves on the left side of the plot corresponding to near-short-circuit conditions are reduced in height compared to the curves on the right side corresponding to near-open-circuit conditions. As the base acceleration level increases, the discrepancy between the short- and open-circuit responses decreases. At

0.1 g RMS, the near-short-circuit velocity response amplitude is approximately 64% that of the near open circuit response. This grows to 79% and 85% at 0.2 and 0.3 g RMS, respectively. This effect is due to the non-ideal nature of the diode bridge rectifier. As the magnitude of the voltage across the diode bridge rises, the diodes act more like ideal switches. Therefore, the efficiency of the rectifier grows with both the base acceleration amplitude, which increases all response signals, as well as the load resistance, which increases steady-state voltage levels. Interestingly, while the near-short-circuit peak power generation will be higher than the

Fig. 11 AC–DC output test data and model at 0.3 g RMS with various load resistance values. Experimental data shown with markers and model predictions shown with curves

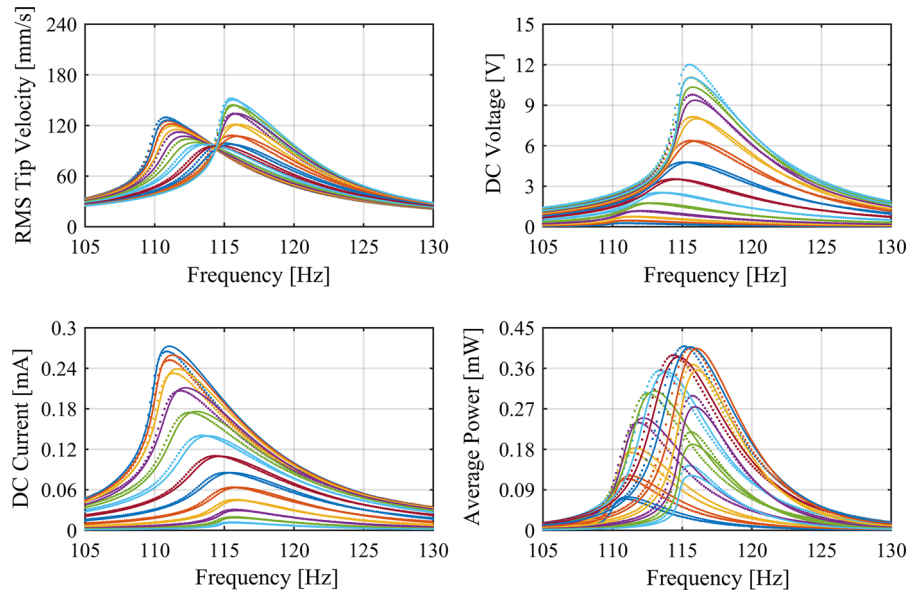


Table 3 Identified parameters for diodes in the bridge rectifier

Saturation current	I_s	1	pA
Ideality factor	n	1	
Thermal voltage	V_T	26	mV

near-open-circuit power generation for a linear piezo-electric cantilever energy harvester due to dielectric losses, the near-open-circuit conditions will produce more power for a practical energy harvester with rectification at finite base acceleration levels.

6 Discussion of the results and basic trends

6.1 Qualitative performance comparisons and trends

It is of interest to understand the effects of the mechanical (elastic and dissipative) and non-ideal electrical (rectification) nonlinearities and their interaction with each other. As a baseline for comparison, the linear regime AC–AC power generation performance can be used. Shown in Fig. 12 is heat map plot of the experimental linear regime power generation performance of the energy harvester normalized by the square of the base acceleration level.

The horizontal and vertical axes correspond to the load resistance value and frequency of base excitation, respectively. Clearly visible are the two maxima

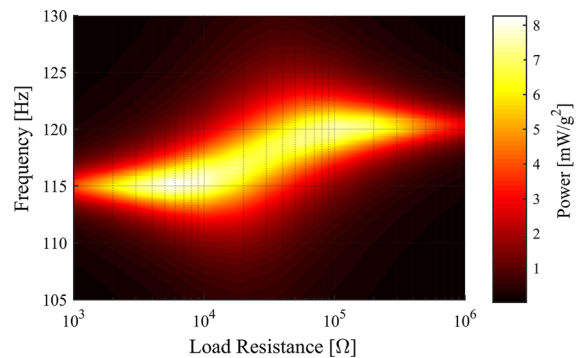
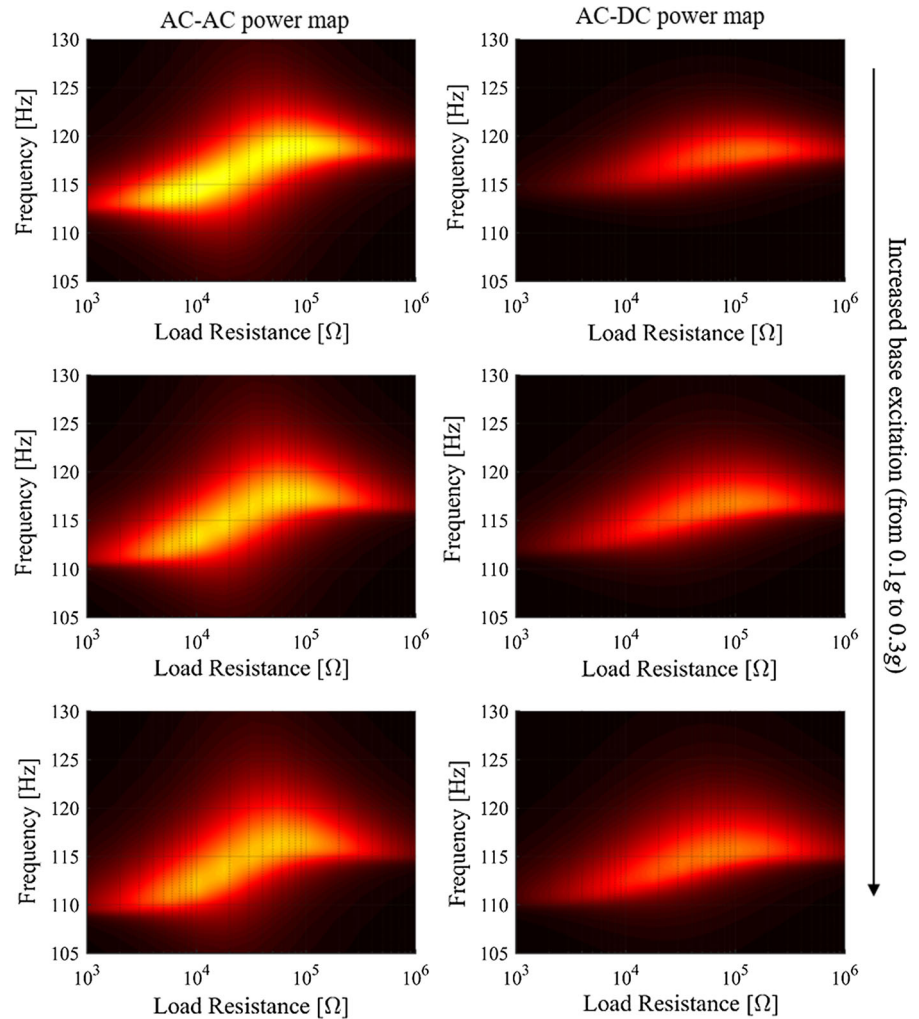


Fig. 12 Heat map of experimental AC–AC energy harvesting performance in the linear regime. Color corresponds to the time-averaged power output of the harvester normalized with respect to the base acceleration level squared

of power generation near the short-circuit and open-circuit loading conditions. The presence of two well-separated peak power points is characteristic of systems with strong electromechanical coupling. In the linear regime, the energy harvester produces a maximum normalized time-averaged power of approximately 8.3 mW/g², and the color of the heat map corresponds to the power output relative to that level. For fair comparisons, the shading in the heat maps for AC–AC and AC–DC performance in the mechanically nonlinear regime are also normalized in this way.

Figure 13 shows an array of six heat maps for the time-averaged power generation. From top to bottom, the rows correspond to the three base accel-

Fig. 13 Heat maps of experimental energy harvesting performance in the mechanically nonlinear regime. From top to bottom, rows correspond to the three tested excitation levels of 0.1, 0.2, and 0.3 g RMS, respectively. The left column corresponds to the AC–AC case, and the right column corresponds to the AC–DC case. Color corresponds to the time-averaged power output of the harvester normalized with respect to the base acceleration level squared. Color is scaled relative to that of the linear regime performance shown in Fig. 12. (Color figure online)



eration levels of 0.1, 0.2, and 0.3 g RMS, respectively. The two columns correspond to the two circuit configurations, with the AC–AC configuration on the left, and the AC–DC configuration on the right. All six heat maps are shaded relative to the 8.3 mW/g^2 maximum normalized mean power generation level of the linear regime performance shown in Fig. 12.

The first apparent trend is that normalized power generation performance is lower in all six mechanically nonlinear regime tests than that of the linear regime, as shown by the darker shades. As was shown with earlier modeling, the dominant mechanical nonlinearities are in the dissipation and stiffness. Power generation performance decreases with increasing mechanical damping, and so the nonlinear mechanical dissipation

reduces the normalized power generation performance as response amplitudes increase at higher excitation levels. The stiffness nonlinearity only affects the magnitude of power generation slightly. Its primary effect is to shift the location of peak power operating points to lower frequencies and higher load resistance values.

Secondly, the power generation performance of the AC–DC configuration is significantly lower than that of the AC–AC configuration. The AC–DC configuration retains the power generation losses due to the nonlinear mechanical dissipation and adds electrical dissipation in the bridge rectifier. An idealized bridge rectifier [42,43] dissipates no power. Ideal diodes act as a perfect conductor for positive bias voltages (no voltage drop), and a perfect insulator for negative bias voltages (no current flow). A real diode bridge does dissipate

power and so reduces the power supplied to the load. Therefore, the linear regime AC–AC power generation performance can be seen as a global upper limit and the mechanically nonlinear AC–AC performance as excitation level specific upper bounds.

The first and second observed trends show that the nonlinear mechanical dissipation reduces relative power generation performance as excitation level increases, and the AC–DC circuit configuration will always have lower absolute performance than the AC–AC configuration due to electrical power dissipation in the diode bridge. However, unlike the AC–AC case, as the base excitation level increases, the normalized power generation performance of the AC–DC configuration improves rather than declines. While losses in the diode bridge are unavoidable, and it never acts like the idealized one-way perfect conductor, the exponential nature of a diode's I–V characteristic means that as the amplitude of the voltage across the piezoelectric electrodes increases, the diode bridge acts more and more ideally. The contribution to the total loss of the diode bridge relative to mechanical dissipation therefore decreases with increasing excitation level. For certain choices of piezoelectric energy harvester and circuit components, the normalized power generation will increase with increasing excitation level as rectification becomes more ideal and then will decrease as nonlinear mechanical dissipation becomes dominant.

Finally, a fourth trend can be seen by examining the linear and mechanically nonlinear power generation performance of the AC–AC circuit configuration. As mentioned earlier, this energy harvester shows two distinct peak power points in the linear response regime, characteristic of a strongly electromechanically coupled system. At the lowest base acceleration level (0.1 g RMS) of the mechanically nonlinear tests, the two peak power points are still visible. However, as the base acceleration level grows to 0.3 g RMS, the two peaks appear to merge and become a single global maximum. This effect is again due to the nonlinear mechanical dissipation. The two high-amplitude responses near-short-circuit and open-circuit conditions are preferentially attenuated compared to the lower-amplitude response at between them. The dip in power generation performance between the near-short-circuit and near-open-circuit conditions therefore disappears as the excitation level increases due to the nonlinear mechanical dissipation.

6.2 Electromechanical response waveforms

One of the benefits of using the method of harmonic balance to solve the nonlinear lumped-parameter models for a practical energy harvester is that it allows the quick simulation of steady-state behavior. From the performance curves and heat maps, the optimal power generation performance of the energy harvester in the practical AC–DC circuit configuration at 0.3 g RMS occurs at approximately 115 Hz, with an optimal load resistance of around 56 k Ω . Simulating these conditions with the method of harmonic balance takes much less computation time than a time domain numerical simulation. Figures 14 and 15 show the model predicted waveforms of the relative tip velocity, piezoelectric electrode voltage, and load voltage. These waveforms are produced from the harmonic balance solution including frequency components up to five times the excitation frequency (i.e., five harmonics were used in the Fourier series expansion of periodic response forms). Notably, the velocity response appears quite sinusoidal, while the piezoelectric electrode voltage, v_p , clearly shows higher harmonic content. The load voltage, v , shows a noticeable amount of ripple. As discussed previously, a filter capacitance somewhat smaller than what would be used in practical energy harvesting circuit was used in this work for experimental reasons. However this example shows highlights the ability of a the method described here to find accurate solutions without making assumptions like a constant output voltage.

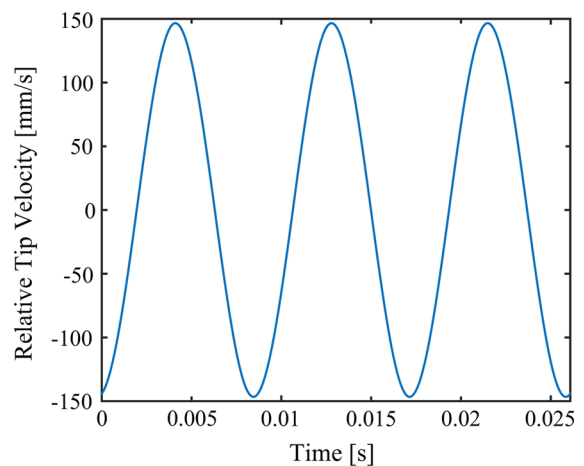


Fig. 14 Representative simulated tip velocity response waveform at 0.3 g RMS base excitation for near optimal load resistance of 56 k Ω and peak power frequency of 115 Hz

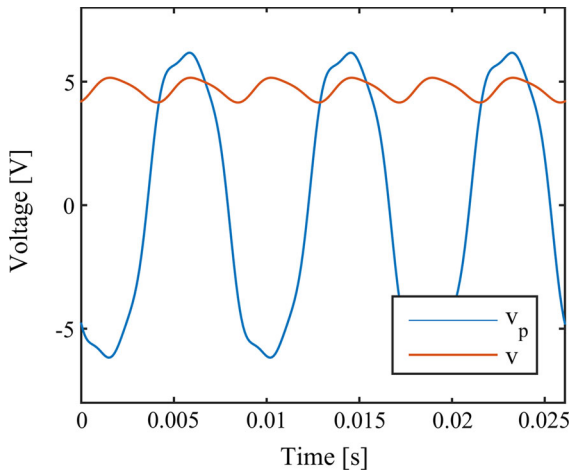


Fig. 15 Representative simulated output voltage, v (red), and piezoelectric electrode voltage, v_p (blue), response waveforms at 0.3 g RMS base excitation for near optimal load resistance of 56 k Ω and peak power frequency of 115 Hz. (Color figure online)

7 Conclusions

A complete representation of resonant piezoelectric energy harvesting requires accounting for mechanical and dissipative nonlinearities as well as the nonlinear process of AC–DC conversion with non-ideal diodes. In this paper, a multiphysics harmonic balance framework was presented by combining these mechanical and electrical nonlinear non-ideal effects to predict the DC electrical output (DC voltage across the load) in terms of the AC mechanical input (base vibration). Focus was placed on a stiff (geometrically linear) bimorph cantilever with piezoelectric laminates connected to a full-wave rectifier and a filter capacitor. The problem was explored first to characterize mechanical nonlinearities by exploring the AC input (base excitation) and AC output (voltage across the load) problem in the presence of a resistive load. Mechanical nonlinearities were identified and validated for different excitation levels. A rectifier comprising non-ideal diodes was then introduced to the system along with a filter capacitor. For the multiphysics equations of the fully coupled nonlinear system, a multi-term harmonic balance solution (with 5 harmonics) was applied to analyze the mechanically and electrically nonlinear system dynamics at different excitation levels. A full set of experiments was conducted, showing trends and interactions of the material softening and dissipative

nonlinearities and the rectification nonlinearities manifested by non-ideal diodes. The multi-term harmonic balance framework can capture the ripple in the DC signal (due to finite filter capacitance) and the overall amplitude-dependent nonlinear dynamics accounting for realistic diode behavior. The experiments validated the proposed modeling method, and highlighted the need for simulating the full nonlinear dynamics of resonant piezoelectric energy harvesters for real world applications with realistic circuit components.

Acknowledgements This work was supported by the National Science Foundation under Grant CMMI-1254262.

Compliance with ethical standards

Conflict of interest The authors declare that they have no conflict of interest.

References

1. Roundy, S., Wright, P.K., Rabaey, J.M.: Energy scavenging for wireless sensor networks. Springer, Berlin (2003)
2. Erturk, A., Inman, D.J.: Piezoelectric Energy Harvesting. Wiley, New York (2011)
3. Elvin, N., Erturk, A.: Advances in energy harvesting methods. Springer, Berlin (2013)
4. Glynne-Jones, P., Tudor, M.J., Beeby, S.P., White, N.M.: An electromagnetic, vibration-powered generator for intelligent sensor systems. *Sensors Actuators A Phys.* **110**(1–3), 344–349 (2004)
5. Arnold, D.P.: Review of microscale magnetic power generation. *IEEE Trans. Magn.* **43**(11), 3940–3951 (2007)
6. Roundy, S., Wright, P.K., Rabaey, J.: A study of low level vibrations as a power source for wireless sensor nodes. *Comput. Commun.* **26**(11), 1131–1144 (2003)
7. Mitcheson, P.D., Miao, P., Stark, B.H., Yeatman, E.M., Holmes, A.S., Green, T.C.: Mems electrostatic micropower generator for low frequency operation. *Sensors Actuators A Phys.* **115**(2–3), 523–529 (2004)
8. Erturk, A., Inman, D.J.: An experimentally validated bimorph cantilever model for piezoelectric energy harvesting from base excitations. *Smart Mater. Struct.* **18**(2), 025009 (2009)
9. Dutoit, N.E., Wardle, B.L.: Experimental verification of models for microfabricated piezoelectric vibration energy harvesters. *AIAA J.* **45**(5), 1126–1137 (2007)
10. Adhikari, S., Friswell, M., Inman, D.: Piezoelectric energy harvesting from broadband random vibrations. *Smart Mater. Struct.* **18**(11), 115005 (2009)
11. Wang, L., Yuan, F.G.: Vibration energy harvesting by magnetostrictive material. *Smart Mater. Struct.* **17**(4), 045009 (2008)
12. Kornbluh, R.D., Pelrine, R., Prahald, H., Wong-Foy, A., McCoy, B., Kim, S., Eckerle, J., Low, T.: From Boats to Buys: Promises and Challenges of Dielectric Elastomer Energy Harvesting, pp. 67–93. Springer, Berlin (2012)

13. Aureli, M., Prince, C., Porfiri, M., Peterson, S.D.: Energy harvesting from base excitation of ionic polymer metal composites in fluid environments. *Smart Mater. Struct.* **19**(1), 015003 (2010)
14. Anton, S., Farinholt, K., Erturk, A.: Piezoelectret foam-based vibration energy harvesting. *J. Intell. Mater. Syst. Struct.* **25**, 1681–1692 (2014)
15. Deng, Q., Kammoun, M., Erturk, A., Sharma, P.: Nanoscale flexoelectric energy harvesting. *Int. J. Solids Struct.* **51**, 3218–3225 (2014)
16. Moura, A.G., Erturk, A.: Electroelastodynamics of flexoelectric energy conversion and harvesting in elastic dielectrics. *J. Appl. Phys.* **121**(6), 064110 (2017)
17. Anton, S.R., Sodano, H.A.: A review of power harvesting using piezoelectric materials (2003–2006). *Smart Mater. Struct.* **16**(3), R1 (2007)
18. Priya, S.: Advances in energy harvesting using low profile piezoelectric transducers. *J. Electroceramics* **19**(1), 167–184 (2007)
19. Cook-Chennault, K.A., Thambi, N., Sastry, A.M.: Powering mems portable devices—a review of non-regenerative and regenerative power supply systems with special emphasis on piezoelectric energy harvesting systems. *Smart Mater. Struct.* **17**(4), 043001 (2008)
20. Elvin, N.G., Elvin, A.A.: A general equivalent circuit model for piezoelectric generators. *J. Intell. Mater. Syst. Struct.* **20**(1), 3–9 (2009)
21. Nayfeh, A.H., Mook, D.T.: *Nonlinear Oscillations*. Wiley, New York (2008)
22. Guckenheimer, J., Holmes, P.: *Nonlinear oscillations, dynamical systems, and bifurcations of vector fields*, vol. 42. Springer, New York (1983)
23. Erturk, A., Hoffmann, J., Inman, D.J.: A piezomagnetoelastic structure for broadband vibration energy harvesting. *Appl. Phys. Lett.* **94**(25), 254102 (2009)
24. Cottone, F., Vocca, H., Gammaitoni, L.: Nonlinear energy harvesting. *Phys. Rev. Lett.* **102**(8), 080601 (2009)
25. Stanton, S.C., McGehee, C.C., Mann, B.P.: Reversible hysteresis for broadband magnetopiezoelectric energy harvesting. *Appl. Phys. Lett.* **95**(17), 174103–174103–3 (2009)
26. Arrieta, A.F., Hagedorn, P., Erturk, A., Inman, D.J.: A piezoelectric bistable plate for nonlinear broadband energy harvesting. *Appl. Phys. Lett.* **97**(10), 104102 (2010)
27. Daqaq, M.F.: Response of uni-modal duffing-type harvesters to random forced excitations. *J. Sound Vib.* **329**(18), 3621–3631 (2010)
28. Litak, G., Friswell, M.I., Adhikari, S.: Magnetopiezoelectric energy harvesting driven by random excitations. *Appl. Phys. Lett.* **96**(21), 214103 (2010)
29. Zhao, S., Erturk, A.: On the stochastic excitation of monostable and bistable electroelastic power generators: relative advantages and tradeoffs in a physical system. *Appl. Phys. Lett.* **102**(10), 103902 (2013)
30. Daqaq, M.F., Masana, R., Erturk, A., Quinn, D.D.: On the role of nonlinearities in vibratory energy harvesting: a critical review and discussion. *Appl. Mech. Rev.* **66**(4), 040801 (2014)
31. Leadenham, S., Erturk, A.: Nonlinear m-shaped broadband piezoelectric energy harvester for very low base accelerations: primary and secondary resonances. *Smart Mater. Struct.* **24**(5), 055021 (2015)
32. Stanton, S.C., Erturk, A., Mann, B.P., Inman, D.J.: Nonlinear piezoelectricity in electroelastic energy harvesters: modeling and experimental identification. *J. Appl. Phys.* **108**(7), 074903 (2010a)
33. Stanton, S.C., Erturk, A., Mann, B.P., Inman, D.J.: Resonant manifestation of intrinsic nonlinearity within electroelastic micropower generators. *Appl. Phys. Lett.* **97**(25), 254101 (2010b)
34. Abdelkefi, A., Nayfeh, A.H., Hajj, M.R.: Effects of nonlinear piezoelectric coupling on energy harvesters under direct excitation. *Nonlinear Dyn.* **67**(2), 1221–1232 (2011a)
35. Abdelkefi, A., Nayfeh, A.H., Hajj, M.R.: Global nonlinear distributed-parameter model of parametrically excited piezoelectric energy harvesters. *Nonlinear Dyn.* **67**(2), 1147–1160 (2011b)
36. Stanton, S.C., Erturk, A., Mann, B.P., Dowell, E.H., Inman, D.J.: Nonlinear nonconservative behavior and modeling of piezoelectric energy harvesters including proof mass effects. *J. Intell. Mater. Syst. Struct.* **23**(2), 183–199 (2012)
37. Leadenham, S., Erturk, A.: Unified nonlinear electroelastic dynamics of a bimorph piezoelectric cantilever for energy harvesting, sensing, and actuation. *Nonlinear Dyn.* **79**(3), 1727–1743 (2015)
38. Tan, D., Yavarow, P., Erturk, A.: Resonant nonlinearities of piezoelectric macro-fiber composite cantilevers with interdigitated electrodes in energy harvesting. *Nonlinear Dyn.* **92**(4), 1935–1945 (2018)
39. Szarka, G.D., Stark, B.H., Burrow, S.G.: Review of power conditioning for kinetic energy harvesting systems. *IEEE Trans. Power Electron.* **27**(2), 803–815 (2012)
40. Guyomar, D., Badel, A., Lefeuvre, E., Richard, C.: Toward energy harvesting using active materials and conversion improvement by nonlinear processing. *IEEE Trans. Ultrason. Ferroelectr. Freq. Control* **52**(4), 584–595 (2005)
41. Rupp, C.J., Dunn, M.L., Maute, K.: Analysis of piezoelectric energy harvesting systems with non-linear circuits using the harmonic balance method. *J. Intell. Mater. Syst. Struct.* **21**(14), 1383–1396 (2010)
42. Shu, Y.C., Lien, I.C.: Analysis of power output for piezoelectric energy harvesting systems. *Smart Mater. Struct.* **15**(6), 1499–1512 (2006)
43. Dai, Q., Harn, R.L.: Charging power optimization for nonlinear vibration energy harvesting systems subjected to arbitrary, persistent base excitations. *Smart Mater. Struct.* **27**(1), 015011 (2017)

Publisher's Note Springer Nature remains neutral with regard to jurisdictional claims in published maps and institutional affiliations.